Supporting Information

Laanait et al. 10.1073/pnas.1214204109

SI Text

1. Molecular Dynamics. *1.1. Simulation setup.* Classical molecular dynamics (MD) are used to describe the chemically specific ion–solvent interactions of the ions enhanced at the interface: Na^+ on the water side and tetrakis(pentafluorophenyl)borate ($TPFB^-$) on the 1,2-dichloroethane (DCE) side. We use the simple point charge (SPC) force field to model the water (1) and a fully flexible DCE force field derived in the work by Benjamin (2) from ab initio calculations and fitting to the empirical data. The combination of the SPC force field and the Benjamin DCE force field leads to a simulated neat water/DCE interface that is in agreement with the experimental interfacial tension (2). In the simulation of Na^+, the water/DCE system was modeled by a rectangular box in the xy plane, with dimensions 50×50 Å; the oil phase extends from $z = 0$ to $z \approx 40$ Å, whereas the aqueous phase reaches $z \approx -26$ Å, with a total of 2,424 water molecules and 844 DCE molecules. The intermolecular interactions are smoothly cut off at distances larger than one-half of the length of the simulation box. The truncation of the long-range behavior of the Coulomb potential is treated using the reaction field correction (3). The simulations were done exclusively in the microcanonical ensemble (constant N, V, E) using a velocity Verlet algorithm to integrate the equations of motion (3) using an integration time step of 1 fs in a custom computer code written by I.B. The simulation boxes are equilibrated to attain a fixed temperature (296 K) using Nosé constant temperature dynamics and velocity rescaling.

1.2. Force fields. The interactions used in the simulation to define the ionic contribution to the system's potential energy are comprised of 6–12 Lennard–Jones parameters, Coulomb interactions, and intramolecular interactions in the case of $TPFB^-$. Lennard–Jones interactions between two atoms i, j in the system were computed using Lorentz–Berthelot mixing rules: $\sigma_{ij} = (\sigma_i + \sigma_j)/2$ and $\epsilon_{ij} = \sqrt{\epsilon_i \epsilon_j}$. Force field parameters of $TPFB^-$ consist of defining the Lennard–Jones parameters (ϵ, σ) for each constituent atom (C, F, and B), partial charges for Coulomb interactions (Table S2), and intramolecular interactions. We consider a fully flexible $TPFB^-$ with bonded interactions characterized by bond stretching and bending treated in the quadratic potential approximation as well as torsion (2). From the crystal structure of $TPFB^-$ (4), equilibrium bond lengths r^{eq} and equilibrium bond angles θ^{eq} entering the force field are determined by averaging over the crystal structure values ($r^{eq}_{BC}, r^{eq}_{CF}, r^{eq}_{CC}, \theta^{eq}_{CBC}, \theta^{eq}_{BCC}$, and θ^{eq}_{CCF} listed in Table S3). The harmonic force constants that define bond stretching and bending, involving combinations of C and F atoms (k_{CF}, k_{CC}, k_{CCF}, and k_{CCC} in Table S3), are readily available from the general Amber force field (5), which was used in the simulations. The bond stretching constant of the C–B bond (k_{BC}) was determined from a vibrational analysis using Gaussian03 (6), and the quantum model was second-order Møller–Plesset perturbation theory in the aug-cc-pVDZ basis. Because boron enters into all bonded interactions that define the geometry of $TPFB^-$ in the simulation, its corresponding parameters (k_{CBC} and k_{CBC}) were set to preserve the equilibrium tetrahedral structure. Consequently, the bending constant of the C–B–C angle was tentatively set to be approximately equal to the constant of its counterpart for the C–C–C, with the equilibrium angle, $\widehat{CBC}$, set to be the angle of a tetrahedral given that the crystal structure average ($\widehat{CBC} = 107.55°$) is very close to that geometry. The torsion potentials, $V_{F–C–C–C}$ and $V_{C–C–B–C}$, are chosen to keep the fluorine atoms in the plane of the flurophenyl rings and maintain the tetrahedral equilibrium configuration, respectively. In Table S3, we summarize the parameters that enter the intramolecular potentials in the quadratic potential approximation to model bonded interactions of $TPFB^-$.

The intramolecular potentials of $TPFB^-$ have a relatively small contribution to the overall ion interaction energy compared with the Coulomb and Lennard–Jones interactions. Hence, accurate parametrization of the latter is necessary, especially for the C and F atoms. The Lennard–Jones parameters for aromatic carbon and fluorine were taken from the Amber force field (7), whereas the Lennard–Jones parameters of boron are taken from the literature (8), which is shown in Table S2. Several Lennard–Jones parameters for C and F were tested, with the ones from the Amber force field producing the best agreement with the experimental free energy of transfer; varying (ϵ_B, σ_B) did not affect the results of the simulation.

The atomic partial charges of $TPFB^-$ (Table S2) were determined from quantum computations using second-order Møller–Plesset perturbation theory in the aug-cc-pVDZ basis using the CHELPG algorithm implemented in the computational chemistry package NWCHEM (9). The CHELPG algorithm consists of assigning a charge q_i to atom i in a molecule and then using a monopole expansion to calculate the resultant electrostatic potential. The values of the partial charges are fitted to minimize the difference between the electrostatic potential and the molecular potential determined from the ab initio computation.

1.3. Solvent interaction potential. We seek to simulate a potential that encompasses an ion's interaction with the solvents present in the system as a function of the interfacial height z. This potential f^{sol} can then be used in Eq. **2** to describe the contribution of intermolecular interactions to the free energy of the electrical double layer. To achieve this result, we use the potential of mean force technique, which is summarized:

- An ion is inserted into an equilibrated simulation box of the neat liquid/liquid interface at a specific z in the bulk liquids.
- The system is then equilibrated for a few hundred picoseconds.
- A simulation run lasting 2 ns ensues, with the ion's position fixed.
- The force acting on the ion's center mass is ensemble-averaged at the end of the simulation, $\langle F^{ion} \rangle_{N,V,E}$.
- The procedure is repeated with the ion placed at a different z position. The heights are chosen from one bulk liquid to the other.
- The ion–solvent interaction is found from the following expression:

$$f^{sol}(z) = -\int dz' \langle F^{ion}(z - z') \rangle_{N,V,E}. \qquad \textbf{[S1]}$$

The above procedure was used for $TPFB^-$, and the simulated averaged force F^{ion} is shown in Fig S1. Fig. 4 shows $f^{sol}_{TPFB^-}$.

2. Numerical Solution of the Poisson Equation. To calculate the ion distributions at the liquid/liquid interface, Poisson's equation with the charge density provided by an electrical double-layer model [Poisson–Boltzmann (PB), PB/MD, and Correlation (CORR)] (Eq. **5**) is applied to both liquid phases, with the interface located at $z = 0$. In all of the models considered in the text, a numerical solution of $\phi(z)$ across the interface is found to satisfy the following boundary conditions:

- Bulk electroneutrality $E|_{z=\pm\infty} = 0$, where $E(z)$ is the electric field.
- Experimental potential drop across the interface: $\phi|_{z=\infty} - \phi|_{z=-\infty} = \Delta\phi$.

- Electric field discontinuity at the interface: $\epsilon_r^w E|_{z=0^+} = \epsilon_r^{DCE} E|_{z=0^-}$.
- Electrostatic potential continuity across the interface: $\phi|_{z=0^+} = \phi|_{z=0^-}$.

The computational package Mathematica (Version 8; Wolfram Research) was used to solve the second-order nonlinear differential equation. Specifically, the built-in functions NDSolve[ ] with the shooting method specified (10) and FindRoot[ ] were used to solve the boundary value problem defined above. Typical numerical errors in the boundary conditions are less than 0.5%. It is noteworthy that our numerical solution of the PB equation compares very well with the exact analytic solution of the latter when it exists, with differences no greater than 10^{-7} V (4).

3. Ion Correlations. ***3.1. Theory.*** The ion distribution theory is outlined in the text. Here, we present the following equations that are required for the numerical computation to determine the ion density profile $n(z)$ and the electric potential $\phi(z)$ self-consistently

$$\overline{n}_-(z) = \int n_-(z')w[|z-z'|; n_-(z)]\mathrm{d}z', \quad [\mathbf{S2}]$$

(Eq. **S3**)

$$w(r) = \frac{3}{2\pi s^2}\left(\frac{1}{r}-\frac{1}{s}\right)\Theta(s-r), \quad [\mathbf{S3}]$$

and (Eq. **S4**)

$$\overline{n}(z) = \frac{3}{2s^3}\int \mathrm{d}z' n(z')(s-|z-z'|)^2, \quad [\mathbf{S4}]$$

where s is the radius of the correlation hole defined by (11)

$$s = \frac{1}{\kappa}(\omega-1), \qquad \omega = \left(1+3\ell_B\kappa\right)^{1/3} = \left(1+(3\Gamma)^{3/2}\right)^{1/3}, \quad [\mathbf{S5}]$$

$\kappa = \sqrt{4\pi n \ell_B}$ is the inverse Debye length, and n is the homogeneous density of the plasma. Eq. **S2** is Eq. **7** in the text, but here, we present Eq. **S3** for the weight function w that was derived in ref. 12. Eq. **S4** is derived on substitution of Eq. **S3** into Eq. **S2**, with the additional consideration that the radial dependence of Eq. **S3** must be projected onto the z axis (13). Eq. **S4** is then used in Eq. **8** in the text along with the following densities

$$\begin{aligned}
n_{\mathrm{Na}^+}(z) &= n^b \exp\left[-\beta\left(e\phi(z)+f^{sol}_{\mathrm{Na}^+}(z)\right)\right],\\
n_{\mathrm{Cl}^-}(z) &= n^b \exp[\beta e\phi(z)],\\
n_{\mathrm{BTPPA}^+}(z) &= n^b \exp[-\beta e\phi(z)],\\
n_{\mathrm{TPFB}^-}(z) &= n^b \exp\left[\beta\left(e\phi(z)-f^{sol}_{\mathrm{TPFB}^-}(z)-\mu^{corr}(z)\right)\right],\\
\mu^{corr}(z) &= \frac{\delta\mathcal{F}^{\mathrm{corr}}}{\delta n_{\mathrm{TPFB}^-}(z)}\\
&= f^{\mathrm{DHH}}(n_{\mathrm{TPFB}^-}(z)) + \int \mathrm{d}z n_{\mathrm{TPFB}^-}(z)\frac{\delta f^{\mathrm{DHH}}(\overline{n}_{\mathrm{TPFB}^-})}{\delta n_{\mathrm{TPFB}^-}}.
\end{aligned} \quad [\mathbf{S6}]$$

3.2. Computation. Given that the excess chemical potential caused by ion correlations in Eq. **S6**, μ^{corr}, depends on n_{TPFB^-} in Eq. **S2** to calculate the ion distributions, Poisson's equation and Eqs. **S4** and **S6** are numerically solved to self-consistency and define what we call the CORR model. The solution to Poisson's equation, the electrostatic potential $\phi(z)$, satisfies the same boundary conditions discussed in *SI Text*, *section 1.1*. The algorithm used to self-consistently solve for the density profiles for the NaCl/bis (triphenylphosphoranylidene) ammonium (BTPPA) TPFB system from the CORR model is described:

- Choose $n^{\mathrm{guess}}_{\mathrm{TPFB}^-}(z)$.
- Find $s(n^{\mathrm{guess}}_{\mathrm{TPFB}^-}(z))$ from Eq. **S5**.
- Compute $\overline{n}_{\mathrm{TPFB}^-}(z)$ from Eq. **S4** with $n_{\mathrm{TPFB}^-}(z) \to n^{\mathrm{guess}}_{\mathrm{TPFB}^-}(z)$.
- Find $f^{\mathrm{DHH}}(\overline{n}_{\mathrm{TPFB}^-}(z))$.
- Compute μ^{corr} from Eq. **S6**.
- Define Poisson's equation with the ion densities given by Eq. **S6**.
- Solve Poisson's equation numerically.
- The numerical solution of Poisson's equation, $\phi(z)$, is used to find $n_{\mathrm{TPFB}^-}(z)$, again using Eq. **S6**.
- If $max\{|n_{\mathrm{TPFB}^-}(z) - n^{\mathrm{guess}}_{\mathrm{TPFB}^-}(z)|\} <$ Tolerance, then the computation has converged.
- If $max\{|n_{\mathrm{TPFB}^-}(z) - n^{\mathrm{guess}}_{\mathrm{TPFB}^-}(z)|\} >$ Tolerance, then $n^{\mathrm{guess}}_{\mathrm{TPFB}^-}(z) \equiv n_{\mathrm{TPFB}^-}(z)$, and the loop is repeated.

A few notes about the above algorithm are that (*i*) the computational procedure does not depend on the starting guess as long as $n^{\mathrm{guess}}_{\mathrm{TPFB}^-}(-\infty) = n^b$ and (*ii*) the code scans a list of differences between the guess and the solution at each z (after the maximum value is found, it is compared with the convergence criterion or the tolerance). We choose a tolerance of 10^{-6}M, which produces an approximate error of 0.1% in n^b used in the computation and less than 10^{-4}% in the maximum value of n_{TPFB^-}.

4. Potential of Zero Charge and Interfacial Excess Charge. Measurements of the potential-dependent interfacial tension, $\gamma(\phi)$, were performed on the system using the Wilhelmy plate method (14), where a Teflon plate is put in wetting contact with the interface. The Teflon plate is attached to a Cahn microbalance, which measures this force per length. The interfacial tension data are shown in Fig. S1. The Lippmann equation allows us to determine the surface excess charge from potential-dependent tension measurements,

$$\sigma = -\left(\frac{\partial\gamma}{\partial\Delta\phi^{\mathrm{w-o}}_{\mathrm{cell}}}\right)_{T,V,\mu}, \quad [\mathbf{S7}]$$

where T is the temperature, V is the volume, and μ is the chemical potential.

The potential of zero charge $\Delta\phi^{pzc}$ is determined by the position on the interfacial tension curve that corresponds to $\sigma = 0$. This potential is used to determine the potential difference $\Delta\phi = \phi_{water} - \phi_{DCE}$ across the liquid/liquid interface under investigation from the measured electrochemical cell potential and the potential of zero charge (pzc), $\Delta\phi = \Delta\phi^{cell} - \Delta\phi^{pzc}$. Note that the electrochemical cell potential is the potential difference across a series of potential drops represented by the electrochemical cell diagram: Ag | AgCl | 10 mM NaCl (water) || 5 mM BTPPATPFB (DCE) | 10 mM LiCl + 1 mM BTPPACl (water) | AgCl | Ag, where || represents the interface under investigation; the other | symbols represent other interfaces in the electrochemical cell. Electrical double layers exist at several of these interfaces, but the standard electrochemical procedure just described allows us to determine the potential difference $\Delta\phi$ across the interface under investigation.

5. X-Ray Reflectivity Data Analysis. To calculate the electron density $\rho(z)$ and R/R_F from the ion density profiles $n_i(z)$, we use the method described in ref. 15. The first step in this method is to define an intrinsic electron density profile, where the solvents are assumed to be homogeneously distributed

$$\rho^{int}_{\text{solvent}}(z) = \begin{cases} \rho_{\text{w}}, & z > 0 \\ \rho_{\text{o}}, & z < 0, \end{cases} \quad \textbf{[S8]}$$

with the following electron densities for water, $\rho_{\text{w}} = 0.333\ \text{e}^{-}/\text{Å}^3$, and DCE, $\rho_{\text{o}} = 0.38\ \text{e}^{-}/\text{Å}^3$. The electron density of the double layer is accounted for by smearing the charge of an ion throughout its volume using a Gaussian function; for this purpose, the ions were modeled as spheres of diameter 1.95 Å for Na^+, 3.66 Å for Cl^-, 11.0 Å for $BTPPA^+$, and 10.0 Å for $TPFB^-$, where the last two were calculated from the crystal structure of BTPPATPFB. At some potential $\Delta\phi$, a theoretical model (in the text) is used to predict a density profile $n_i(z)$ of each ion i present in the system. The overall intrinsic electron density is given by

$$\rho^{int}(z) = \rho^{int}_{\text{solvent}}(z) + \sum_i \left(\overline{n}_i(z) N_i^e - \overline{n}_i(z) V_i \rho^{int}_{\text{solvent}}(z) \right), \quad \textbf{[S9]}$$

where the sum is over the ion types, $\overline{n}_i(z)$ is the size-smeared density profile of ion i, and N_i^e is the number of electrons of ion i. Although the first term in the sum counts the contribution of the ion densities to the electron density profile, the last term subtracts the solvent electron density within the ionic volume V_i to eliminate overcounting of the solvent's electron density. The intrinsic electron density $\rho^{int}(z)$ is not directly measurable by reflectivity. Because of interfacial thermal fluctuations, reflectivity measures fluctuations superposed on the intrinsic electron density profile given in Eq. **S9**. Hence, the relevant electron density profile averaged over the xy plane is given by

$$\langle \rho(z) \rangle_{xy} = \left(\rho^{int} \star \mathcal{N}\left(0, \sigma_{cap}(\phi)\right) \right)(z), \quad \textbf{[S10]}$$

where $\star$ is the convolution operation, and $\mathcal{N}$ is the normal distribution that capillary wave theory assigns to interfacial fluctuations. This theory describes density fluctuations as driven by thermal fluctuations and opposed by surface tension and gravity, and it provides a useful connection between the interfacial tension and rms value of height fluctuations (h_{xy}) or interfacial width, σ_{cap}

$$\sigma^2_{cap}(\phi) \equiv \left\langle h^2_{xy} \right\rangle = \frac{k_B T}{2\pi\gamma(\phi)} \ln \frac{Q^{\max}_{xy}}{Q^{\min}_{xy}}, \quad \textbf{[S11]}$$

where $\gamma(\phi)$ is the potential-dependent interfacial tension (Fig. S1), $Q^{\max}$ represents the maximum wave vector above which a continuum description of fluctuations breaks down (taken to be $\pi/10\ \text{Å}^{-1}$), and $Q^{\min}$ is the in-plane experimental resolution ($\approx 10^{-4}\text{Å}^{-1}$). Because of the dependence of the interfacial width and the ion distributions on the electrostatic potential, the procedure to define $\rho(z)$ is done at each potential. The X-ray reflectivity is calculated by Parratt's method, where the electron density profile is divided up into very small segments along the interfacial normal. The reflection and transmission coefficients can then be exactly calculated in each segment (including the effects of absorption), and the reflectivity is then obtained over the entire domain of electron density variation. Fitting of calculated reflectivity R^{cal} to measured data R used only the interfacial roughness (Table S1) [Q_z offset ($\approx 10^{-4}\text{Å}^{-1}$, which represents a typical misalignment of the reflectometer)]. The quality of the fit was determined by the χ^2 value, defined by

$$\chi^2 = \frac{1}{n-2} \sum_i \left(\frac{R(Q_{z,i}) - R^{cal}(Q_{z,i})}{\sigma_i} \right)^2, \quad \textbf{[S12]}$$

where the sum is over the distinct Q_z points measured, n is the total number of data points, and σ is the uncertainty in the measured reflected signal.

1. Berendsen HJC, Postma JPM, van Gunstersen WF, Hermans J (1981) Interaction models for water in relation to protein hydration. *Intermolecular Forces*, ed Pullman B (Reidel, Dordrecht), pp 331–342.
2. Benjamin I (1992) Theoretical study of water/1,2-dichloroethane interface: Structure, dynamics and conformation equilibrium at the liquid-liquid interface. *J Chem Phys* 97: 1432.
3. Allen MP, Tildesley DJ (1987) *Computer Simulation of Liquids* (Clarendon, Oxford).
4. Laanait N (2011) Ion correlations at electrified soft matter interfaces. PhD thesis (University of Illinois, Chicago, IL).
5. Wang J, Wolf RM, Caldwell JW, Kollman PA, Case DA (2004) Development and testing of a general Amber force field. *J Comput Chem* 25(9):1157–1174.
6. Frisch MJ, et al. (2004) *Gaussian 03* (Gaussian, Inc., Wallingford, CT).
7. Cornell W, et al. (1995) A second generation force field for the simulation of proteins, nucleic acids, and organic molecules. *J Am Chem Soc* 117:5179–5197.
8. Firlej L, Kuchta B, Wexler C, Pfeifer P (2009) Boron substituted graphene: Energy landscape for hydrogen adsorption. *Adsorption* 15:312–317.
9. Valiev M, et al. (2010) Nwchem: A comprehensive and scalable open-source solution for large scale molecular simulations. *Comput Phys Commun* 181:1477.
10. Sofroniu M, Knapp R (2008) Advanced numerical differential equation solving. *Mathematica*, Wolfram Mathematica Tutorial Collection (Wolfram Research, Inc.).
11. Nordholm S (1984) Simple analysis of the thermodynamic properties of the one-component plasma. *Chem Phys Lett* 105:302.
12. Groot RD (1991) Ion condensation on solid particles: Theory and simulations. *J Chem Phys* 95:9191.
13. Diehl A, Tamashiro MN, Barbosa MC, Levin Y (1999) Density-functional theory for attraction between like-charged plates. *Physica A* 274:433–445.
14. Adamson AW (1990) *Physical Chemistry of Surfaces* (Wiley, New York), 5th Ed.
15. Luo G, et al. (2006) Ion distributions at the nitrobenzene-water interface electrified by a common ion. *J Electroanal Chem (Lausanne Switz)* 593:142–158.

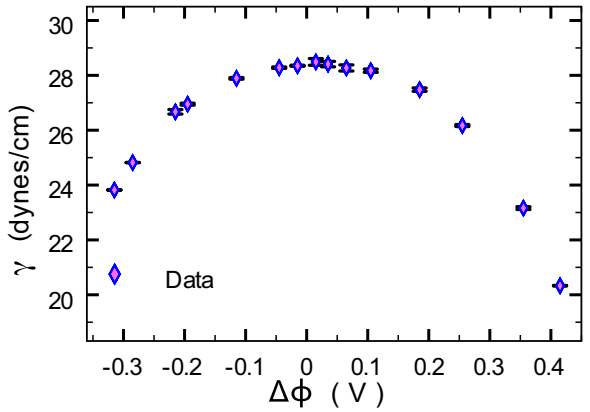

Fig. S1. Potential-dependent interfacial tension, $\gamma(\phi)$, measured using a Wilhelmy plate method at the water/1,2-dichloroethane interface. Note that the measurements are originally made as a function of the cell potential $\Delta\phi^{cell}$, but they are plotted as a function of $\Delta\phi = \Delta\phi^{cell} - \Delta\phi^{pzc}$, where $\Delta\phi^{pzc}$ was determined to be 0.374 V by the point at which $\sigma = 0$.

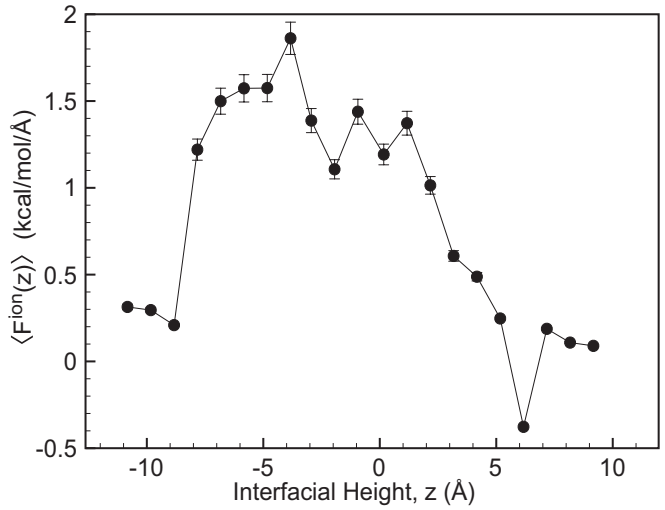

Fig. S2. MD simulated average force $\langle F^{ion}\rangle_{N,V,E}$ acting on the center of mass of $TPFB^-$. Each data point is the result of a 2-ns simulation run with the ion's position fixed at the corresponding interfacial height.

Table S1. X-ray fitted roughness and capillary wave theory values

	Capillary wave theory (Å)	CORR (±0.20 Å)	PB/MD (±0.20 Å)
$\Delta\phi = 0.406$ V	5.23	4.91	4.91
$\Delta\phi = 0.346$ V	4.92	4.53	4.53
$\Delta\phi = 0.286$ V	4.74	4.30	4.30
$\Delta\phi = 0.246$ V	4.61	4.32	4.35
$\Delta\phi = 0.174$ V	4.54	4.21	4.09
$\Delta\phi = 0.006$ V	4.44	4.38	4.40

Table S2. Partial charges and Lennard–Jones parameters for $TPFB^-$

Atom	σ (Å)	ε (kcal/mol)	q (e)
F	3.50	0.061	−0.145199
C	3.816	0.086	0.079332
B	3.543	0.095	1.2×10^{-5}

Table S3. Parameters of bonded interactions of $TPFB^-$

Parameter	Value
k_{BC}	631.74 kcal/mol Å^2
r_{BC}^{eq}	1.66 Å
k_{CF}	368.70 kcal/mol Å^2
r_{CF}^{eq}	1.35 Å
k_{CC}	589.70 kcal/mol Å^2
r_{CC}^{eq}	1.38 Å
k_{CBC}	100.0 kcal/mol rad^{-2}
θ_{CBC}^{eq}	109.47°
k_{BCC}	200.0 kcal/mol rad^{-2}
θ_{BCC}^{eq}	113.4°
k_{CCF}	67.8 kcal/mol rad^{-2}
θ_{CCF}^{eq}	119.50°
k_{CCC}	69.8 kcal/mol rad^{-2}
θ_{CCF}^{eq}	120.0°
$V_{F-C-C-C}$	9 kcal/mol
$V_{C-C-B-C}$	90 kcal/mol